Dimension-Controllable Microtube Arrays by Dynamic Holographic Processing as 3D Yeast Culture Scaffolds for Asymmetrical Growth Regulation

Shengyun Ji, Liang Yang, Yanlei Hu, Jincheng Ni, Wenqiang Du, Jiawen Li, Gang Zhao, Dong Wu,* and Jiaru Chu*

***T**ransparent microtubes can function as unique cell culture scaffolds, because the tubular 3D microenvironment they provide is very similar to the narrow space of capillaries in vivo. However, how to realize the fabrication of microtube-arrays with variable cross-section dynamically remains challenging. Here, a dynamic holographic processing method for producing high aspect ratio (≈20) microtubes with tunable outside diameter (6–16 μm) and inside diameter (1–10 μm) as yeast culture scaffolds is reported. A ring-structure Bessel beam is modulated from a typical Gaussian-distributed femtosecond laser beam by a spatial light modulator. By combining the axial scanning of the focused beam and the dynamic display of holograms, dimension-controllable microtube arrays (straight, conical, and drum-shape) are rapidly produced by two-photon polymerization. The outside and inside diameters, tube heights, and spatial arrangements are readily tuned by loading different computer-generated holograms and changing the processing parameters. The transparent microtube array as a nontrivial tool for capturing and culturing the budding yeasts reveals the significant effect of tube diameter on budding characteristics. In particular, the conical tube with the inside diameter varying from 5 to 10 μm has remarkable asymmetrical regulation on the growth trend of captured yeasts.*

1. Introduction

Cells embedded in tissues grow in complex 3D microenvironments containing multiple extracellular matrix (ECM) components. However, previous understanding of cell behaviors, including cell migration, directed mitosis, and differential growth is mainly based on studies of cells cultured on flat, 2D commercial culture substrates.[1–3] In recent years, the results of cell behavior studies in 3D culture scaffolds have revealed several differences from that in 2D substrates, such as neurite outgrowth,[4] neural stem cell migration,[5] and tumor cell division.[6] Therefore, biocompatible 3D culture scaffolds which can more closely mimic the natural complex 3D microenvironment in vivo are urgently needed.

Microtubes, which have very high aspect ratio with variable diameter in nano- and micrometer scale, have almost universal applications in areas as diverse as micro-optics,[7–9] resonators,[10–12] microrobots,[13,14] microscale energy storage,[15] micromedical devices,[16,17] and microbiology.[4–6,18–20] Especially in the field of microbiology, microtube array has great potential as a powerful tool to research the biological mechanisms in 3D culture environment because of the dissimilarity between 2D flat surfaces and 3D

S. Y. Ji, Dr. L. Yang, Prof. Y. L. Hu, J. C. Ni, W. Q. Du, Prof. J. W. Li, Prof. G. Zhao, Prof. D. Wu, Prof. J. R. Chu
CAS Key Laboratory of Mechanical Behavior and Design of Materials
Department of Precision Machinery and Precision Instrumentation
University of Science and Technology of China
Hefei, Anhui 230027, China
E-mail: huyl@ustc.edu.cn; dongwu@ustc.edu.cn
Prof. Y. L. Hu, Prof. D. Wu
Department of Precision Machinery and Instrumentation
University of Science and Technology of China
Hefei, Anhui 230027, China

DOI: 10.1002/smll.201701190

extracellular environments in which cells routinely operate in vivo.[1–3,21] Recently, hydrogels composed of fibrillar proteins have been employed to study the cellular behaviors in a 3D environment.[22,23] However, it still remains challenging to determine the pure impact of environment dimensionality on cell behaviors due to the porosity and compliance of hydrogel scaffold. To address this challenge, microtubes have been used to demonstrate how the tubular confinements of 3D scaffolds affect budding yeast growth,[18] neuron cell growth,[4,19] neural stem cell migration mechanism,[5] human cancer cell division, and differentiation.[6,20] However, further studies are still urgent to be carried out to assess the contribution of more complex 3D culture scaffolds to the cellular behaviors, for instance, conical tubular environment.

For studying the cellular behaviors in 3D microenvironment, microtubes made of biocompatible materials are highly desirable. A number of methods, including self-assembling,[24,25] self-rolled-up,[26,27] templating,[28] electrospinning,[29–32] lithography,[33] and direct laser writing,[34] have been developed to fabricate different types of microtubes of varying scales. However, the processing flexibility has yet to be improved, because some of these methods could only produce microtubes with specific shapes or rough surface in fixed patterns, or some processes are complicated or inefficient.

Femtosecond laser microfabrication by two-photon polymerization (TPP) shows sufficient flexibility in producing complex 3D microstructures with high resolution.[35–38] There have been some 3D microstructures realized by TPP used as 3D cell culture scaffolds for studying cell behaviors, for instance, cage-like structures for studying cell invasion[39,40] and quadrilateral bracket structure functionalized with distinct ECM proteins for guiding cell attachment.[41] However, the efficiency of traditional laser direct writing 3D microstructures needs to be improved. With the development of spatial light modulation technology, the light field can be flexibly regulated.[42] The combination of the two technologies allows for the enhanced flexibility and efficiency for producing complex 3D structures. The ring-shaped microstructures have been realized by holographic modulation of the annular light field.[43,44] However, as cell culture scaffolds, the aspect ratio and maneuverability of the microtubes need to be further improved. To the best of our knowledge, microtubes produced by femtosecond laser two-photon polymerization combined with spatial light modulation have not yet been used for studying the cellular behaviors in 3D cell culture scaffolds.

In this study, we present a dynamic holographic processing method to fabricate high aspect ratio (≈20) microtubes with tunable outside diameter (6–16 μm) and inside diameter (1–10 μm). The influence of tuning topological charge n and axicon radius r_0 of computer-generated holograms (CGHs) on the geometrical shape and size of microstructures is discussed in detail. A self-falling-down method is demonstrated to construct transparent microtube arrays consisting of 100 single tubes for capturing and culturing yeast cells. This strategy exhibits great flexibility and high reliability because the average retention rate and survival rate of captured yeasts can both reach more than 70%. Moreover, we analyze the effects of 2D tubular confinements of different microtubes, including straight microtube arrays (the inside diameter ranging from 3 to 10 μm) and conical microtube arrays (the inside diameter varying from 5 to 10 μm), on the yeast growth characteristics by high-resolution bright-field microscopy. This method holds great promise for studying the cellular behaviors in 3D extracellular environment by mimicking the microenvironment in vivo.

2. Results and Discussion

2.1. Tunable Bessel Beams Generation and Their Utilization in Microtubes Fabrication

Figure 1a illustrates the experimental setup for controllable microtube fabrication based on spatial light modulator (SLM). The ring-structure Bessel beam[45] is modulated by a CGH displayed on the SLM.[46–48] The CGH is composed of three parts: spiral phase plate (SPP), axicon, and blazed grating (BG), as shown in Figure 1b. SPP has an azimuthal phase distribution of $n\varphi$ and its topological charge n is an integer and represents the order of Bessel beam. Axicon has a radial phase distribution of $2\pi r/r_0$, r_0 is the radius of the axicon. The topological charge n and the axicon radius r_0 of this CGH is 5 and 400 μm, respectively. Finally, the phase distribution of BG is expressed by $2\pi x/\Delta$, in which Δ represents the period of the blazed grating (15 × 8 μm). Therefore, the final phase distribution of the CGH can be presented as:

$$Ph(x,y) = \mathrm{mod}\left(n\varphi + 2\pi r/r_0 + 2\pi x/\Delta, 2\pi\right) \quad (1)$$

where $Ph(x, y)$ is the phase distribution in Cartesian coordinate, $\varphi = \tan^{-1}(y/x)$ is the polar angle, and $r = \sqrt{x^2 + y^2}$ is the polar radius. BG phase is a quite important part to separate the zeroth order light, due to the pixelation effect of the SLM, from the other modulated light, as shown in Figure 1c. Thus only the 1st order light of the modulated beam can pass through an iris diaphragm (with an intermediate aperture of 8 mm) used as a filter. Then the filtered light beam is focused by a high numerical aperture (NA = 1.35) 60× oil-immersion objective lens to form a controllable ring-structure light field by loading CGHs with different topological charge n and axicon radius r_0 on the SLM.

Furthermore, to elucidate the consistency of experimental results and simulation, the Debye diffraction theory is adopted to simulate the focused Bessel beams (Figure 1d, the detail will be discussed in next part) generated by the CGH in Figure 1b. First, a light field in the x–z plane is simulated, and the x–y plane light field at seven different z-axis positions is intercepted. Then the line plot of the intensity distribution of two positions (Z_0 and Z_1) is shown in the top right of Figure 1d, where the intensity is sufficient for TPP. By contrast, the size of the double-ring microstructure, fabricated by moving a 10 μm thick SZ2080 photoresist[49] sample along the propagation direction of the focused beam, is in good agreement with the size of the optical field.

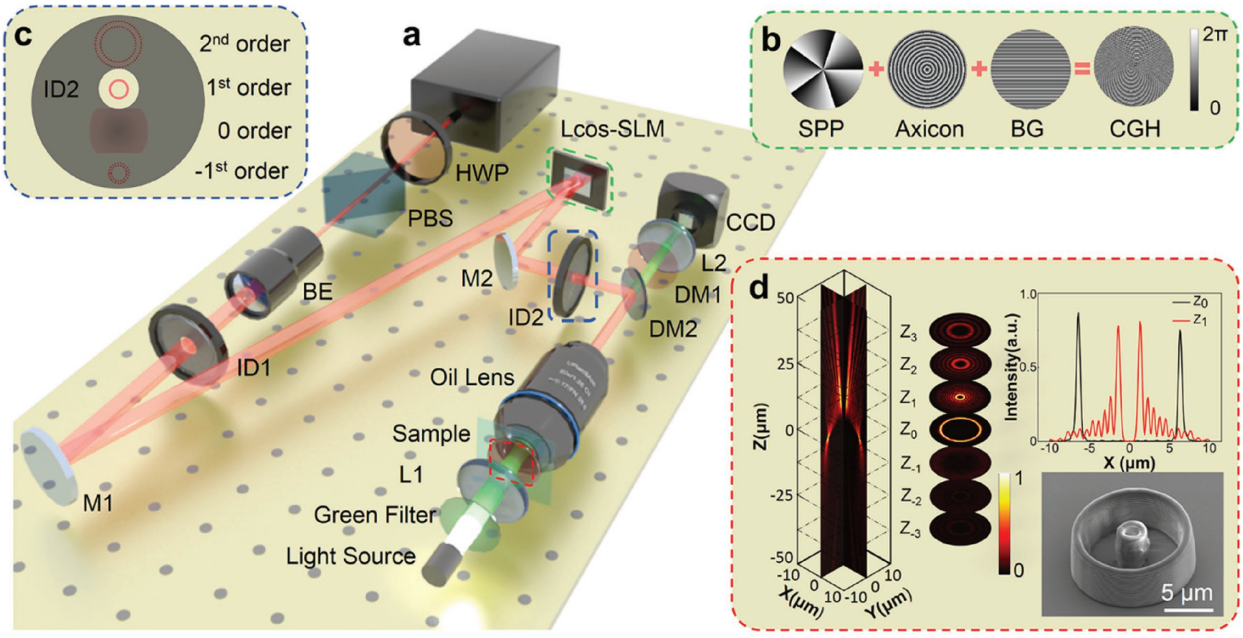

Figure 1. Rapid fabrication of controllable microtubes based on Lcos-SLM. a) Experimental setup. HWP, half wave plate; PBS, polarizing beam splitter; BE, beam expander; ID, Iris diaphragm; M, mirror; Lcos-SLM, liquid-crystal-on-silicon spatial light modulator; L, lens; DM, dielectric mirror; CCD, charge-coupled device. b) Illustration of the computer-generated hologram (CGH) with topological charge $n = 5$, axicon radius $r_0 = 400$ μm, and BG period $\Delta = 15$ μm. c) Iris diaphragm used as a filter to separate the 1st order beam from the other modulated light. d) 3D slice model of simulated light field ($n = 5$ and $r_0 = 400$ μm) under a high numerical aperture (NA = 1.35) oil-immersion objective lens by applying Debye diffraction theory (left). The vertical intensity distribution of the simulated light field in x–y plane in two positions: Z_0 and Z_1 (top right). 45° tilted SEM of double-ring microstructure fabricated in a few seconds by scanning a 10 μm thick sample along the z direction (tens of minutes by singe-point scanning) with the same modulated beam (bottom right).

2.2. Simulation and Reconstruction of Focused Light Field

To provide deeper insights into the variation of the TPP microtubes, the focused light fields under the high NA objective lens modulated from a series of CGHs with different parameters have been simulated (**Figure 2**a). These CGHs have a similar axicon radius of 400 μm, but their topological charge n changes from 0 to 25 successively. First, since the BG phase is added to eliminate the zero-order light caused by the pixelation effect of the SLM and does not influence the phase modulation of the Bessel beam, it is not necessary to consider this part in the simulation. Thus the reflective light of the Gaussian beam after SLM modulation can be describe as:

$$E_0(r,\varphi)=\begin{cases} A_0\exp\left(-r^2/\omega^2\right)\exp\left(i\cdot\mathrm{mod}\right. & 0<r\le R, \\ \left.(n\varphi+2\pi r/r_0,2\pi)\right), & 0<\theta\le\theta_{\max}; \\ 0, & \text{else} \end{cases} \quad (2)$$

where A_0 is a normalized constant, ω is a radius related parameter of Gaussian beam, and R is the maximum radius of the CGH loaded on the SLM. Furthermore, $\theta_{\max} = \sin^{-1}(\mathrm{NA}/n)$, where n is the refractive index of the oil. Combining with the Fresnel diffraction theory, the diffracted field at the entrance pupil (r_1, φ_1, z_1) of the oil-immersion lens, the distance from SLM is z_1, could be described with the Fresnel diffraction integral expressed as:[46]

$$E_1(r_1,\varphi_1,z_1)=A_1\frac{\exp(ikz_1)}{i\lambda z_1}\exp\left(\frac{ikr_1^2}{2z_1}\right)\exp\left[in\left(\varphi_1-\frac{\pi}{2}\right)\right]$$
$$\times\int_0^R\exp\left(-\frac{r^2}{\omega^2}\right)\cdot\exp\left(\frac{ikr^2}{2z_1}\right) \quad (3)$$
$$\cdot\exp\left(-\frac{i2\pi r}{r_0}\right)\cdot J_n\left(\frac{krr_1}{z_1}\right)\cdot rdr$$

where A_1 is a normalized constant, k is the wave number of the incidence, λ is the wavelength of the incidence, and J_n is the nth order Bessel function of the first kind. According to vectorial diffraction theory, the electric field vector near the focal spot can be obtained from the generalized Debye integral as:[50]

$$\vec{E}_2(r_2,\varphi_2,z_2)=\begin{bmatrix} E_x\cdot\hat{x} \\ E_y\cdot\hat{y} \\ E_z\cdot\hat{z} \end{bmatrix}=iC\begin{bmatrix} \hat{x}\hat{y}\hat{z} \end{bmatrix}$$
$$\times\int\int_\Omega\sin(\theta)\cdot E_1(r,\varphi,z_1)\cdot\sqrt{\cos\theta}$$
$$\cdot\begin{bmatrix} 1+(\cos\theta-1)\cos^2\varphi & (\cos\theta-1)\cos\varphi\sin\varphi & -\sin\theta\cos\varphi \\ (\cos\theta-1)\cos\varphi\sin\varphi & 1+(\cos\theta-1)\sin^2\varphi & -\sin\theta\sin\varphi \\ \sin\theta\cos\varphi & \sin\theta\sin\varphi & \cos\theta \end{bmatrix} \quad (4)$$
$$\cdot\begin{bmatrix} p_x \\ p_y \\ p_z \end{bmatrix}\cdot\exp\left\{ik\left[z_2\cos\theta+r_2\sin\theta\cos(\varphi-\varphi_2)\right]\right\}\mathrm{d}\theta\mathrm{d}\varphi$$

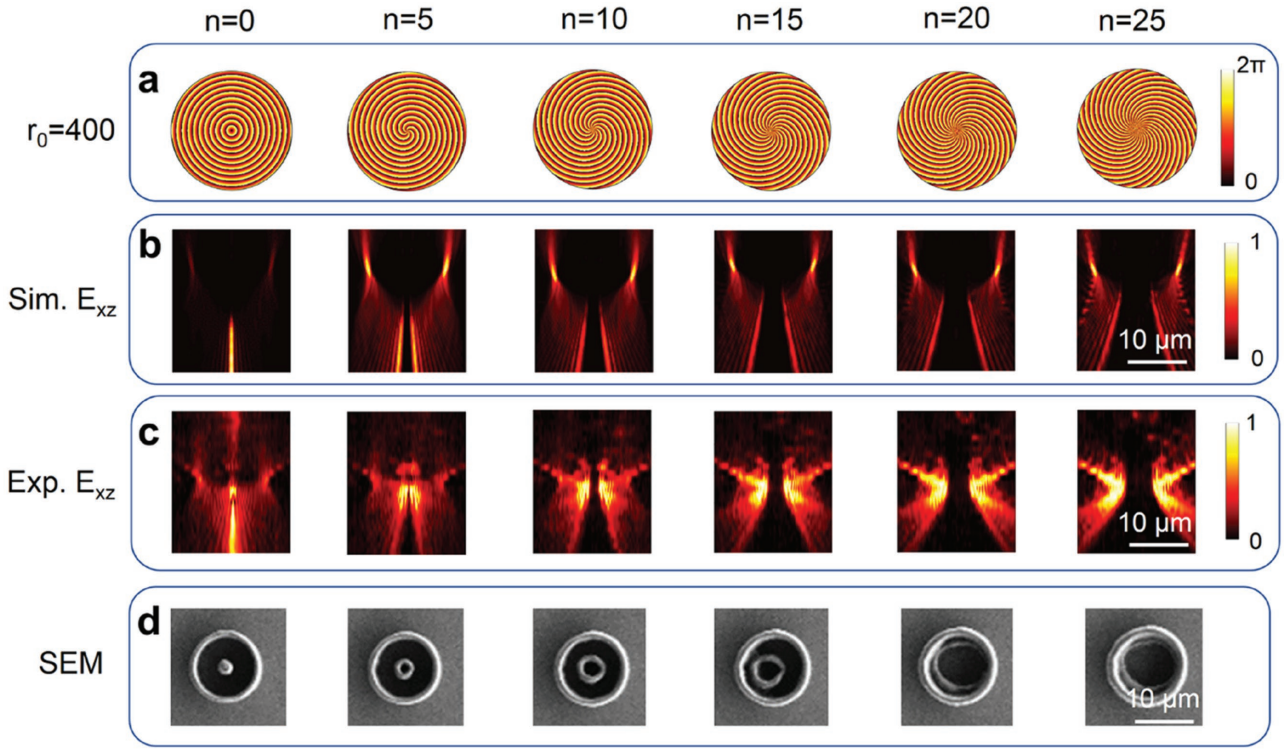

Figure 2. Simulated and experimental light field under high NA objective lens. a) A series of CGHs with different topological charge n = 0, 5, 10, 15, 20, 25 and the same axicon radius r_0 = 400 μm. b) The simulated and c) experimental light field of these CGHs under high NA objective lens in x–z plane. Due to ignoring aberrations and other factors, there are some differences between the simulated light field and the reconstructed light field. d) Top-view SEM images of microstructures with a height of ≈10 μm fabricated by these modulated laser beams.

where $\vec{E}_2(r_2, \varphi_2, z_2)$ is the electric field vector at the point (r_2, φ_2, z_2) expressed in cylindrical coordinates with their origin at the focal point, $\hat{x}, \hat{y}, \hat{z}$ are the unit vectors along the x, y, z directions, C is a normalized constant, and [p_x, p_y, p_z] is a matrix unit vector about the polarization of input light. Due to the elongated shape of the liquid crystal molecules and their birefringence, only the horizontally polarized part of the light is modulated. Therefore, the polarization of the incident beam is adjusted to horizontal linear polarization and the matrix unit vector is [1; 0; 0]. Considering the polarization effects under tight focusing conditions,[51] the effect of the polarization of the incident beam on the focused Bessel beam light field is demonstrated in Figure S9 (Supporting Information). Thus we can obtain the simulated light field by using the numerical integration (Figure 2b). To some extent, the simulation of light field explains the phenomenon of the processing results, how a double-ring structure gradually becomes a single-ring structure, as shown in Figure 2d. However, there are some differences between the simulated light field and the reconstructed light field (Figure 2c) due to ignoring aberrations and other misalignments of optical system.

2.3. Dynamic Holographic Processing of Various Diameter-Varying Microtubes

The parameters of CGHs could significantly affect the morphology of the light field. Therefore, we systematically studied the geometrical characteristics of the microtubes in detail. As the SPP order changes from 0 to 40 (5 for the interval) as well as varying axicon radius from 400 to 900 μm (100 μm for the interval), the size of modulated Bessel beams also changes accordingly (Video S1, Supporting Information). In order to fabricate high quality microtubes for all the CGHs, the TPP energy threshold, and processing speed have been investigated over several experiments (Figure S1, Supporting Information).

Figure 3a shows the scanning electron microscopy (SEM) image of microtubes with all the parameters (for high-resolution SEM, see Figure S2, Supporting Information). First, these microtubes can be divided into three types according to their geometric shape: I, pillar-in-a-ring; II, single-ring; III, double-ring. The first type of microtubes are produced by zero-order Bessel beams modulated from the holograms of SPP order n equals to 0, and the rest are fabricated by high-order Bessel beams. The second type of microtubes (single-ring shape) is the most, which was fabricated by CGHs with high SPP order (more than 5) and large axicon radius (larger than 500 μm). High aspect ratio structures of the first and the third type are shown in Figure S3 (Supporting Information). Second, judging from the geometric size, the diameter of microtubes is positively correlated with topological charge n and negatively correlated with axicon radius r_0. Detailed statistics about the outside diameter and inside diameter of the single-ring microtubes are shown in Figure 3b,c, respectively. Through this method, we can easily and efficiently fabricate high quality microtubes with the outside diameter ranging from about 6 to 16 μm and the inside diameter ranging from

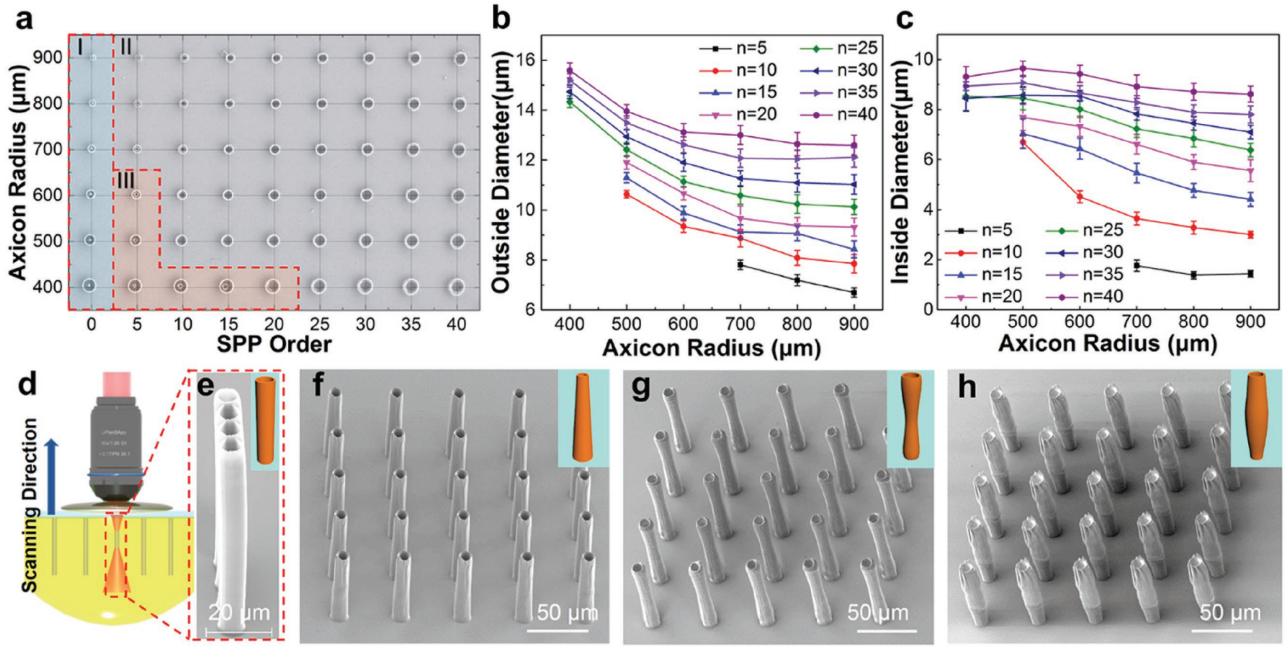

Figure 3. Dynamic holographic processing of various diameter-varying microtubes. a) Dependence of different types of microstructures on SPP order and axicon radius. I, pillar-in-a-ring (the blue area); II, single-ring (the gray area); III, double-ring (the orange area). Quantitative study on b) the outside diameter and c) the inside diameter of the single-ring microstructures as a function of axicon radius and SPP order. d) Schematic illustration of the holographic processing of a microtube array. e) 45° tilted SEM of straight microtube arrays. f) Conical and g,h) drum-shape microtube arrays (the outside diameter varying from 8 to 14 μm and the inside diameter varying from 5 to 10 μm) are produced by dynamic holographic processing, which were challenging for other fabrication methods.

about 1 to 10 μm. If we use an appropriate beam reducer or low magnification objective, a wider range diameter of the microtubes could be obtained.

It should be noted that the length of the microtube, fabricated by moving the thick sample adhered to piezoelectric platform along the *z* direction (Figure 3d), could be as long as the working distance of the oil-immersion lens (150 μm). So through this method, the aspect ratio could be as high as 20 or even more. Furthermore, if holograms with continuously varying parameters are loaded on the SLM during the movement of piezoelectric platform, microtubes with variable cross-section could be successfully produced. Through this dynamic holographic processing method, conical and drum-shape microtube with the inside diameter varying from 5 to 10 μm and outside diameter varying from 8 to 14 μm, or even more complex shapes, can be fabricated, as shown in Figure 3e–h. The inside and outside diameter-varying ratio, defined as the ratio of the maximum diameter to the minimum diameter, is 2 and 1.75, respectively. It is worth mentioning that these complex microtubes are challenging for other fabrication methods which are suitable for microtubes with the same diameter.[26–33] In addition, the fabrication time for a 150 μm high microtube with a scanning speed of 30 μm s^{-1} along the longitudinal direction is only 5 s, which is much shorter than that (tens of minutes) by singe-point scanning, and the total time for fabricating a tube array consisting of 100 single tubes is less than 10 min or even less. Therefore, this processing method can fabricate high aspect ratio transparent microtube arrays with complex shapes reliably and efficiently, opening up a potential for studying the cellular behaviors in complex 3D environment which is more similar to the environment in vivo.

Although this processing method has sufficient flexibility and high processing efficiency, there are still some limitations. The geometry of the microtubes is dictated by the Bessel beam intensity profile. For fabricating microtubes with more complex shapes or other arbitrary 3D microstructures, the modulation of arbitrary light field with high-resolution remains challenging. In order to further enhance the flexibility and efficiency, multibeam parallel processing combined with other forms of analytical light field such as vortex beam and Airy beam, may be an effective method. Moreover, due to the large area of the focused Bessel beam, the laser power to induce TPP for fabricating microtubes (about 70–150 mW, in Figures S1 and S2, Supporting Information) is much higher than the single spot scanning method (about 7 mW for the focused Gaussian beam under the same oil-immersion objective lens). In the processing of straight microtubes, high quality tubes could be produced by adjusting the laser power and scanning speed. In our experiments, it is difficult to obtain high structural strength and low surface roughness of the microtubes with large cross-sectional diameter variation at the same time (Figure S4, Supporting Information). However, high quality fabrication of this kind of microtubes can be expected, if some energy compensation methods are adopted here.

2.4. Construction of Transparent Microtube Arrays as 2D Confined Scaffolds for Yeasts Capture

In recent years, there have been many studies on the growth characteristics of mammalian cells on 2D substrates.[52–55]

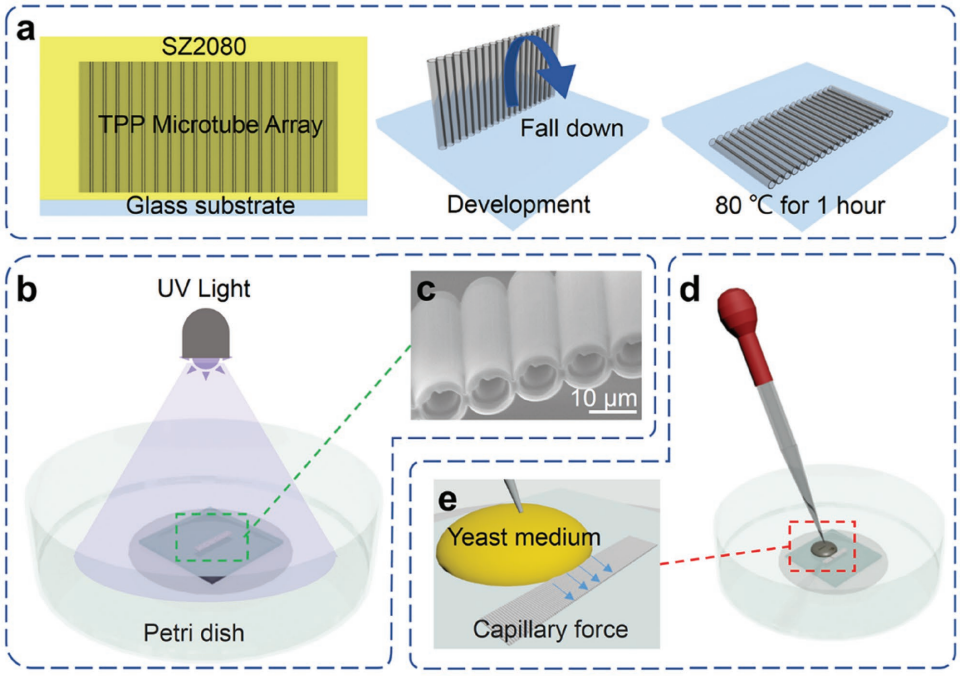

Figure 4. Construction of transparent microtube array as 3D culture scaffolds for yeasts capture. a) Schematic diagram for the construction of transparent microtube arrays by self-fall-down process. b) Illustration of sterilization treatment for the prepared sample under UV light. c) Tilted SEM image of a straight microtube array. d) Illustration of the siphon method to realize yeast capturing by e) capillary force.

However, the growth environment of cells in vivo is mainly in 3D microenvironments, in which the cell growth behaviors are different from that in 2D substrates. Therefore, we could construct polymer-microtube-arrays as tubular 3D microenvironment for studying cell behaviors.

A reliable process method was adopted, as shown in **Figure 4**, to construct transparent microtube arrays to mimic the in vivo microenvironment. This method is composed of three parts: scaffold processing, sterilization treatment, and yeast capturing and culturing. In the first part, the TPP fabrication of producing microtube array composing of 100 single tubes is the same as the method shown in Figure 3d, except that the starting position of the fabrication (the focal plane of the light field) is slightly higher than the interface between the glass and the photoresist (Figure 4a (left)). After the development, the microtube array would fall down by itself. When the developer was completely evaporated, the sample was washed with alcohol and a drop of polydimethylsiloxane (PDMS) was used to attach the sample to a Petri dish. In the second part, the prepared sample was sterilized for 1 h under UV light. In the last part, we adopted siphon method to realize yeast capturing. A few drops of high concentration yeast culture medium were added to the end of microtube array, so that yeasts would be captured into the microtubes by capillary force. A representative movie that demonstrates how a single yeast is captured into the microtube is provided in Video S2 (Supporting Information). Then the yeasts that have not been captured are rinsed off with the culture medium. Finally, the growth and budding process of captured yeasts is observed in situ with a charge-coupled device (CCD) camera for 10 h in 5 mL culture medium.

During the experiments, we found that when the inside diameter of the microtube was more than 6 μm, the capture efficiency could reach 70% or even more (Figure S5, Supporting Information). After uncaptured yeasts were rinsed off with the culture medium, most of the captured yeasts were still remained in the microtubes (Video S3, Supporting Information). Therefore, it is a simple and reliable method to capture the yeast at a high concentration and to study the growth characteristics in different tubular confined microenvironments.

2.5. Growth Characteristics of Yeasts in Microtube Arrays with Different Diameters

Tubular confinement is primarily 2D constraints on 3D cultured yeasts, such microenvironment will affect the area, aspect ratio, and growth angle of the yeast, as shown in **Figure 5**a. The area and aspect ratio of a single yeast is defined as the area and ratio of the major and minor axes of an ellipse fitted to the yeast (by ImageJ), respectively. The growth angle is defined as the angle between the longitudinal direction of mother-daughter yeasts and the perpendicular direction of the microtube. To assess the effects of varying levels of spatial confinement on growth characteristics of yeast, we tuned the diameters of the microtubes by changing different CGHs (referred to Figure 3c) during the fabrication process.

A series of microtube arrays (about 135 μm high) with the inside diameter ranging from 3 μm (smaller than the diameter of non-budding yeast) to 9 μm (larger than the diameter of mature yeast grown in free space) were fabricated for yeasts culturing. The optical transparency of the photoresist material enables the high-resolution microscopic

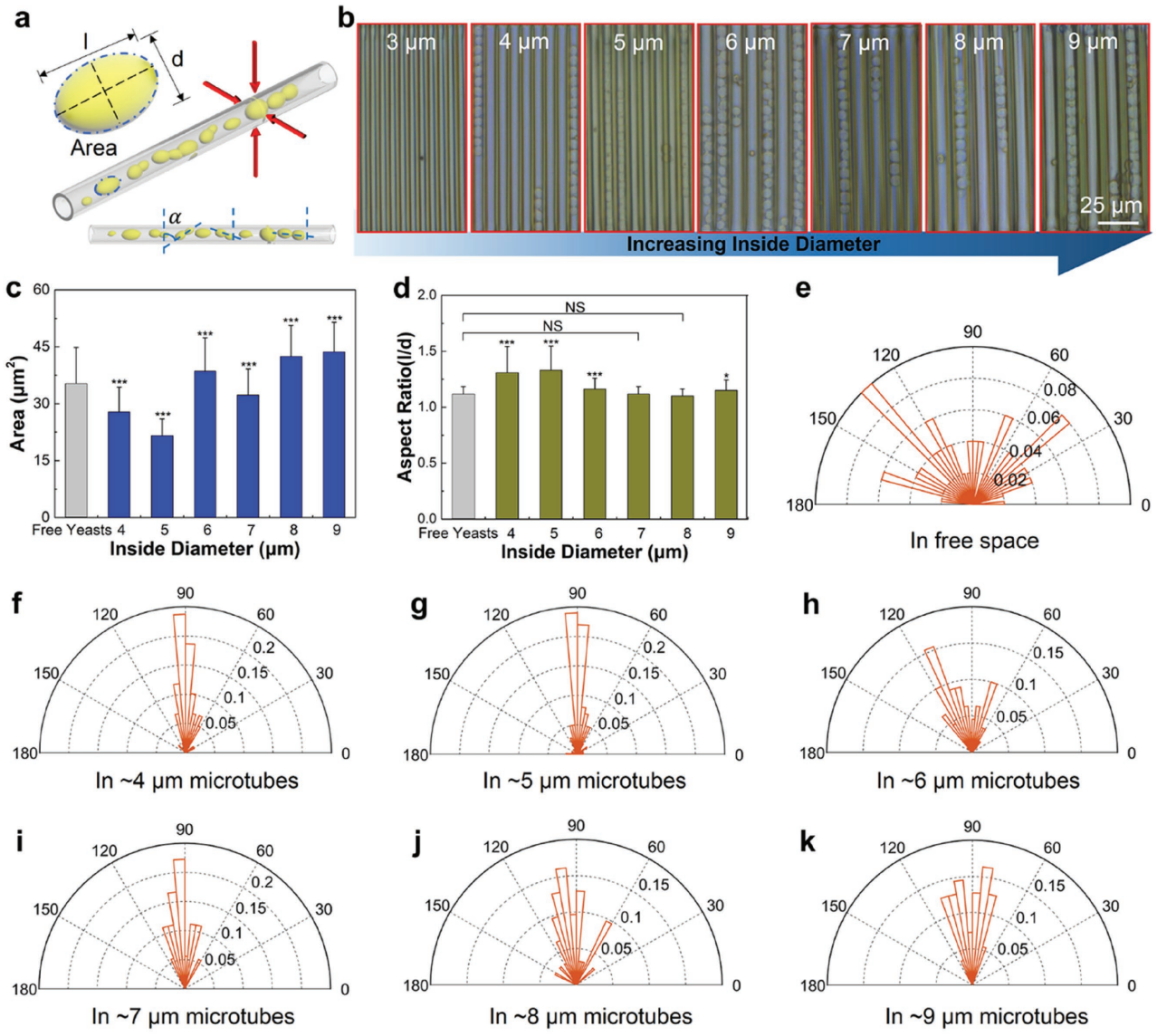

Figure 5. Growth characteristics of yeasts in microtube arrays with different diameters. a) 3D schematic of tubular confinement, indicating 2D constraints (red arrows) on 3D cultured yeasts. The area and aspect ratio are defined as the area and ratio of the major and minor axes (l/d) of an ellipse fitted to the yeast, respectively. b) Bright field microscopy images of yeasts in different diameters of microtube arrays (about 135 μm high) after 10 h of budding process. c) Quantification of areas ± SD in the indicated spatial environments (n = 50, 51, 100, 102, 84, 27, and 50 yeasts from left to right). The mean area of the yeasts in 2D confined microtubes was significantly different from that of the free yeasts. d) Bar graph illustrating aspect ratios ± SD of yeasts in indicated spatial environments (n = 50, 51, 100, 102, 84, 27, and 50 yeasts from left to right). The aspect ratio of yeasts in 4–6 μm sized tube arrays were significant compared to the free yeasts. e–k) The wind rose diagrams illustrating the relative frequency distribution of the growth angle of yeasts budding division (n = 50, 59, 100, 110, 18, 31, and 55 yeasts from (e) to (k)). NS, not significant, *p < 0.05, **p < 0.01, and ***p < 0.001 significantly altered changes compared to free cells (Student's t-test).

observation of yeasts growing inside the polymer scaffolds. The bright field microscope images of yeasts after 10 h of budding process in different diameters of microtube arrays are shown in Figure 5b. The combined bright-field microscope image of the captured yeasts in a microtube array composed of 100 single tubes with the inside diameter of 6 μm is shown in Figure S6 (Supporting Information). To probe how the tubular confinement affects the yeasts, the statistical data of the growth characteristics are obtained (for details see Table S1 in Supporting Information), which contains the area, aspect ratio and growth angle (Figure 5c–k). Since the diameter of the microtube with an inside diameter of 3 μm is so small that almost no yeast is captured in the array, the statistical results are only relevant about the inner diameter ranging from 4 to 9 μm.

We observed that most of the captured yeasts survived in the tube arrays (Figure S7, Supporting Information). Moreover, the mean area of the yeasts in 2D confined microtubes was significantly different from the mean area of the yeasts outside of the microtubes (named "free yeasts") (p-value < 0.001, Student's t test). Due to the narrow space of the tube array with the inside diameter of 4 and 5 μm, the yeast area (27.8 ± 6.6 μm^2 and 21.6 ± 4.4 μm^2) was quite smaller than that of the free yeasts. In addition, an interesting phenomenon was observed: the yeast

area in 8–9 μm microtubes (42.5 ± 8.1 μm^2 and 43.6 ± 7.8 μm^2) was larger than that of free yeasts (35.2 ± 9.5 μm^2). The possible biological mechanism is speculated that: due to the 2D space constraints, the yeast could not complete the budding process quickly, so that the yeast budding time would become longer making the yeast size increased to a certain degree (Figure S8, Supporting Information).

On the other hand, the aspect ratio of yeasts in 4–6 μm sized tube arrays (1.31 ± 0.23, 1.33 ± 0.21, and 1.16 ± 0.10) was significant (p-value < 0.001, Student's t test) compared with free yeasts (1.12 ± 0.07) and the reason is quite simple: when the diameter of the yeasts in the narrow tube increased to the inside diameter of the tube but did not reach the normal transverse split size, so it could only continue to grow longitudinally. As the inner diameter of the tube increased to 7–9 μm, the aspect ratio of the yeast (≈1.1) became almost the same as that of the free yeasts. Finally, the wind rose diagram (Figure 5e–k) shows the relative frequency distribution of the growth angle of budding division. The growth angle of the yeasts inside the tube arrays was limited to a certain angle (90° ± 30°) compared with the random distribution of free yeasts. As the inside diameter of the tube increases, the angular distribution gradually tends to be randomly distributed in a larger angle range.

2.6. Asymmetrical Growth Tendency and Morphological Characteristics of Single Yeast in Conical Microtube

To further study the growth characteristics of the captured yeasts in more complex 2D confined environment, conical microtube arrays (about 135 μm high) as yeast culture scaffolds were fabricated through dynamic holographic processing method, as shown in **Figure 6**b. The cyan dash dot line indicates the initial position of the yeasts and the two yellow dash dot lines indicate the upward and downward growth tendency of the yeasts, respectively. Compared with the yeasts in straight tube with a diameter of 6 μm (Figure 6a; Video S4, Supporting Information), the yeasts in conical tube with the inside diameter varying from 5 to 10 μm showed distinct asymmetric growth property (Video S5, Supporting Information), because the inclined tube wall of conical tube allows the yeasts to grow tendentiously in the large-diameter direction.

Furthermore, the morphological characteristics of yeasts in the upper and lower parts of the cyan dash dot line in both straight and conical tube were compared (for details see Table S2 in Supporting Information). For the conical tube, both the area (p-value < 0.01, Student's t test) and aspect ratio (p-value < 0.01, Student's t test) of the yeasts in the

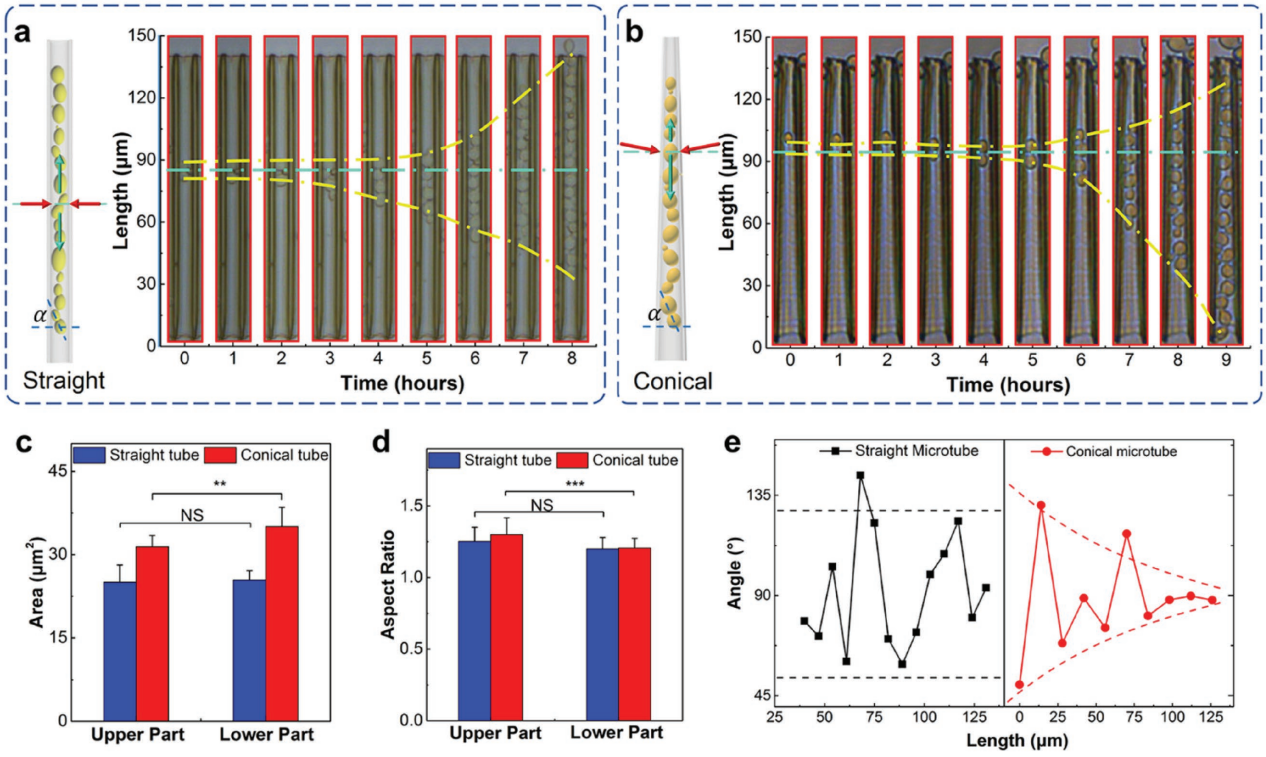

Figure 6. Asymmetrical growth tendency and morphological characteristics of single yeast in conical microtube. a) Schematic diagram of the tubular confinement of straight microtube, indicating the impact of 2D constraints (red arrows) on the growth tendency (cyan arrows) of budding direction (left). Time-lapse images (0–8 h) of a yeast dividing along the length direction inside a straight microtube with the inside diameter of 6 μm (right). b) Illustration of the tubular confinement of conical microtube, indicating the impact of more complex 2D constraints (red arrows) on the growth tendency (cyan arrows) of budding direction (left). Time-lapse images (0–9 h) of a yeast dividing along the length direction inside a conical microtube (about 135 μm high) with the inside diameter varying from 5 to 10 μm (right). (Cyan dash dot line: the initial position of the yeasts; yellow dash dot line: the upward and downward growth tendency.) Bar graph illustrating c) areas ± SD and d) aspect ratios ± SD of yeasts in the indicated area. e) Line chart illustrating the yeasts growth angle in straight (left) and conical microtube (right). NS, not significant, *p < 0.05, **p < 0.01, and ***p < 0.001 significantly altered changes compared to free cells (Student's t-test).

upper part were significantly different from the lower part, while for the straight tube, there were no significant difference between the two parts in either area or aspect ratio (Figure 6c,d). The growth angle of the yeasts in straight and conical tube is shown in Figure 6e. In contrast to the straight tube, it is obvious to conclude that the conical tube becomes more restrictive to the yeast growth angle as its diameter becomes smaller.

3. Conclusion

In summary, an efficient approach to fabricate diameter-varying microtube arrays (straight, conical, and drum-shape) is developed by dynamic holographic femtosecond (fs) laser processing. The microtube arrays were used as transparent 3D yeast culture scaffolds to study the effect of 2D tubular confinement on the growth characteristics of budding yeast. The growth tendency and morphological characteristics of yeasts in the microtube was found to have a significant correlation with the diameter of the tubes. Especially in conical microtubes, the captured yeasts showed distinct asymmetrical growth tendency. This strategy of fabricating diameter-varying microtube arrays with more complex shapes for studying the yeast growth characteristics provides an alternative for microtubes to integrate functionality as biocompatible scaffolds in lab-in-a-tube systems. We believe that this processing method combined with new biological materials has great potential in the area of cell biology and biological tissue engineering.

4. Experimental Section

Fabrication of Microtubes: A typical femtosecond laser direct writing system combined with spatial light modulation technology was used for producing microtubes, in which a Ti:sapphire laser oscillator (Chameleon Vision-S, Coherent Corp., central wavelength: 800 nm, repetition rate: 80 MHz, pulse width: 75 fs) was used as the light source and a reflection type liquid crystal SLM (Pluto NIR II, Holoeye, 1920 × 1080 pixels, 256 gray levels, pixel pitch of 8 μm) was used as the light modulator by loading designed CGHs. A 60× oil-immersion objective (Olympus) with high NA (1.35) was used to focus the modulated ring-structure Bessel beam, which was filtered to obtain the 1st order beam with an iris (with an intermediate aperture of 8 mm), inside the photosensitive material. A commercially available zirconium–silicon hybrid sol–gel material doped with 4,4′-bis(diethylamino)-benzophenone photoinitiator at 1% by weight (SZ2080, IESL-FORTH) was used for photopolymerization, which is negligibly shrinkable compared with other photoresists.[49] The movement of the sample was mainly controlled by a piezoelectric nanopositioning stage (Physik Instrument, P545) with a nanometer resolution and a 200 × 200 × 200 μm moving range. The scanning speed adopted in the processing of the microtubes is 30 μm s^{-1} and the laser power range for the microstructures with different parameters is 50 to 150 mW (for details see Figure S2 in Supporting Information for details). Taking the intensity of a Bessel beam ($n = 25$, $r_0 = 600$) for example, the 120 mW of average optical power (measured before the objective) results in the 0.36 TW cm^{-2} intensity/irradiance; transmission of the optical elements was taken into account.[56] After polymerization, the sample was developed in 1-propanol for 1 h until all of the unpolymerized parts were washed away. The sample was then removed from the developer and the microtube structure could be obtained by spontaneously evaporating the developer. The sample was then washed with alcohol and placed on a Petri dish with a drop of PDMS (Dow Corning, USA). Then the sample was dried on an 80 °C hot plate for 1 h to adhere to the Petri dish.

Imaging Characterization: The SEM images were taken with a secondary electron scanning electron microscope (FEI Sirion200) operated at 10 kV, after the samples were sputter coated with Au for 120 s. The capture process and the yeasts growth process were observed by using a Leica DMI3000B microscope.

Yeast Capture and Culture: In the culture experiment, *Saccharomyces cerevisiae*, a kind of budding yeast (ANGEL YEAST CO., LTD) was used. The liquid culture medium was prepared by sterilizing the mixture of solid granular Granular Sabouraud's Glucose broth medium (Peptone 10.0 g L^{-1}, Glucose 40 g L^{-1}, pH-value 5.6 ± 0.2 at 25 °C, QingDao Hope Bio-technology CO., LTD) and distilled water with a concentration of 50 g L^{-1} at 120 °C for 15 min. The high concentration yeast medium was produced by dissolving 0.1 g dry yeast uniformly into 15 mL liquid culture medium. After the yeasts that had not been captured were rinsed off with the culture medium, 5 mL culture medium was added into the Petri dish. Then the captured yeasts were cultured overnight at 25 °C.

Quantitative Analysis of Yeast Growth Characteristics: Quantitative analysis was implemented by outlining the contour of every identifiable yeast manually using Fiji/ImageJ (National Institutes of Health). Student's *t*-tests were performed to evaluate statistical differences between two groups. The statistical significance was defined as $*p < 0.05$, $**p < 0.01$, and $***p < 0.001$.

Supporting Information

Supporting Information is available from the Wiley Online Library or from the author.

Acknowledgements

This work was supported by the National Natural Science Foundation of China (Nos. 51675503, 61475149, 51405464, 61675190, and 51605463), the Fundamental Research Funds for the Central Universities (Nos. WK2480000002 and WK2090000011), the China Postdoctoral Science Foundation (Nos. 2016M590578 and 2016M602027), Chinese Academy of Sciences Instrument Project (YZ201566), and "Chinese Thousand Young Talents Program" and Youth Innovation Promotion Association CAS (2017495).

Conflict of Interest

The authors declare no conflict of interest.

[1] B. M. Baker, C. S. Chen, *J. Cell Sci.* **2012**, *125*, 3015.
[2] P. Friedl, E. Sahai, S. Weiss, K. M. Yamada, *Nat. Rev. Mol. Cell Biol.* **2012**, *13*, 743.
[3] A. D. Doyle, R. J. Petrie, M. L. Kutys, K. M. Yamada, *Curr. Opin. Cell Biol.* **2013**, *25*, 642.
[4] M. R. Yu, Y. Huang, J. Ballweg, H. Shin, M. H. Huang, D. E. Savage, M. G. Lagally, E. W. Dent, R. H. Blick, J. C. Williams, *ACS Nano* **2011**, *5*, 2447.
[5] B. Koch, A. K. Meyer, L. Helbig, S. M. Harazim, A. Storch, S. Sanchez, O. G. Schmidt, *Nano Lett.* **2015**, *15*, 5530.
[6] W. Xi, C. K. Schmidt, S. Sanchez, D. H. Gracias, R. E. Carazo-Salas, R. Butler, N. Lawrence, S. P. Jackson, O. G. Schmidt, *ACS Nano* **2016**, *10*, 5835.
[7] W. L. Hu, Y. K. Chen, H. Jiang, J. G. Li, G. Zou, Q. J. Zhang, D. G. Zhang, P. Wang, H. Ming, *Adv. Mater.* **2014**, *26*, 3136.
[8] J. X. Zhan, H. X. Dong, S. L. Sun, X. D. Ren, J. J. Liu, Z. H. Chen, C. Lienau, L. Zhang, *Adv. Opt. Mater.* **2016**, *4*, 126.
[9] Y. P. Rakovich, S. Balakrishnan, J. F. Donegan, T. S. Perova, R. A. Moore, Y. K. Gun'ko, *Adv. Funct. Mater.* **2007**, *17*, 1106.
[10] E. J. Smith, S. Schulze, S. Kiravittaya, Y. F. Mei, S. Sanchez, O. G. Schmidt, *Nano Lett.* **2011**, *11*, 4037.
[11] S. Kietzmann, C. Strelow, L. Tavares, J. P. Penttinen, T. V. Hakkarainen, A. Schramm, A. Osadnik, A. Lützen, J. K. Hansen, A. Mews, T. Kipp, *ACS Photonics* **2015**, *2*, 1532.
[12] K. Dietrich, C. Strelow, C. Schliehe, C. Heyn, A. Stemmann, S. Schwaiger, S. Mendach, A. Mews, H. Weller, D. Heitmann, T. Kipp, *Nano Lett.* **2010**, *10*, 627.
[13] M. Guix, J. Orozco, M. García, W. Gao, S. Sattayasamitsathit, A. Merkoçi, A. Escarpa, J. Wang, *ACS Nano* **2012**, *6*, 4445.
[14] Y. F. Mei, A. A. Solovev, S. Sanchez, O. G. Schmidt, *Chem. Soc. Rev.* **2011**, *40*, 2109.
[15] J. W. Deng, X. Y. Lu, L. X. Liu, L. Zhang, O. G. Schmidt, *Adv. Energy Mater.* **2016**, *6*, 1600797.
[16] Z. L. Xiang, H. Wang, A. Pant, G. Pastorin, C. K. Lee, *Biomicrofluidics* **2013**, *7*, 26502.
[17] M. Shin, S. G. Park, B. C. Oh, K. Kim, S. Jo, M. S. Lee, S. S. Oh, S. H. Hong, E. C. Shin, K. S. Kim, S. W. Kang, H. Lee, *Nat. Mater.* **2017**, *16*, 147.
[18] G. S. Huang, Y. F. Mei, D. J. Thurmer, E. Coric, O. G. Schmidt, *Lab Chip* **2009**, *9*, 263.
[19] P. Froeter, Y. Huang, O. V. Cangellaris, W. Huang, E. W. Dent, M. U. Gillette, J. C. Williams, X. L. Li, *ACS Nano* **2014**, *8*, 11108.
[20] W. Xi, C. K. Schmidt, S. Sanchez, D. H. Gracias, R. E. Carazo-Salas, S. P. Jackson, O. G. Schmidt, *Nano Lett.* **2014**, *14*, 4197.
[21] M. J. Blewitt, R. K. Willits, *Ann. Biomed. Eng.* **2007**, *35*, 2159.
[22] Y. Tsuda, Y. Morimoto, S. Takeuchi, *Langmuir* **2010**, *26*, 2645.
[23] J. L. Leight, E. Y. Tokuda, C. E. Jones, A. J. Lin, K. S. Anseth, *Proc. Natl. Acad. Sci. USA* **2015**, *112*, 5366.
[24] R. F. Silva, D. R. Araujo, E. R. Silva, R. A. Ando, W. A. Alves, *Langmuir* **2013**, *29*, 10205.
[25] Q. Li, Y. Jia, L. Dai, Y. Yang, J. B. Li, *ACS Nano* **2015**, *9*, 2689.
[26] O. G. Schmidt, K. Eberl, *Nature* **2001**, *410*, 168.
[27] K. Kumar, B. Nandan, P. Formanek, M. Stamm, *J. Mater. Chem.* **2011**, *21*, 10813.
[28] J. B. Gilbert, J. S. O'Brien, H. S. Suresh, R. E. Cohen, M. F. Rubner, *Adv. Mater.* **2013**, *25*, 5948.
[29] Y. Yu, L. Gu, C. B. Zhu, P. A. van Aken, J. Maier, *J. Am. Chem. Soc.* **2009**, *131*, 15984.
[30] H. Y. Chen, N. Wang, J. C. Di, Y. Zhao, Y. L. Song, L. Jiang, *Langmuir* **2010**, *26*, 11291.
[31] A. Sitt, J. Soukupova, D. Miller, D. Verdi, R. Zboril, H. Hess, J. Lahann, *Small* **2016**, *12*, 1432.
[32] I. Bonadies, F. Cimino, C. Carfagna, A. Pezzella, *Biomacromolecules* **2015**, *16*, 1667.
[33] X. H. Tan, T. L. Shi, Y. Gao, W. J. Sheng, B. Sun, G. L. Liao, *J. Micromech. Microeng.* **2014**, *24*, 055006.
[34] E. Stankevicius, T. Gertus, M. Rutkauskas, M. Gedvilas, G. Raciukaitis, R. Gadonas, V. Smilgevicius, M. Malinauskas, *J. Micromech. Microeng.* **2012**, *22*, 065022.
[35] S. Kawata, H. B. Sun, T. Tanaka, K. Takada, *Nature* **2001**, *412*, 698.
[36] D. Wu, J. Xu, L. G. Niu, S. Z. Wu, K. Midorikawa, K. Sugioka, *Light: Sci. Appl.* **2015**, *4*, e228.
[37] M. Malinauskas, A. Žukauskas, S. Hasegawa, Y. Hayasaki, V. Mizeikis, R. Buividas, S. Juodkazis, *Light: Sci. Appl.* **2016**, *5*, e16133.
[38] L. J. Jiang, W. Xiong, Y. S. Zhou, Y. Liu, X. Huang, D. W. Li, T. Baldacchini, L. Jiang, Y. F. Lu, *Opt. Express* **2016**, *24*, 13687.
[39] A. M. Greiner, M. Jäckel, A. C. Scheiwe, D. R. Stamow, T. J. Autenrieth, J. Lahann, C. M. Franz, M. Bastmeyer, *Biomaterials* **2014**, *35*, 611.
[40] B. Spagnolo, V. Brunetti, G. Leménager, E. De Luca, L. Sileo, T. Pellegrino, P. P. Pompa, M. De Vittorio, F. Pisanello, *Sci. Rep.* **2015**, *5*, 10531.
[41] B. Richter, V. Hahn, S. Bertels, T. K. Claus, M. Wegener, G. Delaittre, C. Barner-Kowollik, M. Bastmeyer, *Adv. Mater.* **2017**, *29*, 1604342.
[42] A. M. Weiner, *Rev. Sci. Instrum.* **2000**, *71*, 1929.
[43] C. C. Zhang, Y. L. Hu, J. W. Li, G. Q. Li, J. R. Chu, W. H. Huang, *Opt. Express* **2014**, *22*, 3983.
[44] L. Yang, A. El-Tamer, U. Hinze, J. W. Li, Y. L. Hu, W. H. Huang, J. R. Chu, B. N. Chichkov, *Appl. Phys. Lett.* **2014**, *105*, 041110.
[45] J. Durnin, *J. Opt. Soc. Am. A* **1987**, *4*, 651.
[46] J. A. Davis, E. Carcole, D. M. Cottrell, *Appl. Opt.* **1996**, *35*, 593.
[47] A. Vasara, J. Turunen, A. T. Friberg, *J. Opt. Soc. Am. A* **1989**, *6*, 1748.
[48] N. Chattrapiban, E. A. Rogers, D. Cofield, W. T. Hill, R. Roy, *Opt. Lett.* **2003**, *28*, 2183.
[49] A. Ovsianikov, J. Viertl, B. Chichkov, M. Oubaha, B. MacCraith, I. Sakellari, A. Giakoumaki, D. Gray, M. Vamvakaki, M. Farsari, C. Fotakis, *ACS Nano* **2008**, *2*, 2257.
[50] X. Hao, C. F. Kuang, T. T. Wang, X. Liu, *J. Opt.* **2010**, *12*, 115707.
[51] S. Rekštytė, T. Jonavičius, D. Gailevičius, M. Malinauskas, V. Mizeikis, E. G. Gamaly, S. Juodkazis, *Adv. Opt. Mater.* **2016**, *4*, 1209.
[52] M. K. Driscoll, X. Y. Sun, C. Guven, J. T. Fourkas, W. Losert, *ACS Nano* **2014**, *8*, 3546.
[53] G. Kumar, C. C. Ho, C. C. Co, *Adv. Mater.* **2007**, *19*, 1084.
[54] M. Thery, V. Racine, A. Pepin, M. Piel, Y. Chen, J. B. Sibarita, M. Bornens, *Nat. Cell Biol.* **2005**, *7*, 947.
[55] C. S. Chen, M. Mrksich, S. Huang, G. M. Whitesides, D. E. Ingber, *Science* **1997**, *276*, 1425.
[56] L. Jonušauskas, D. Gailevičius, L. Mikolių naitė, D. Sakalauskas, S. Šakirzanovas, S. Juodkazis, M. Malinauskas, *Materials* **2017**, *10*, 12.

Received: April 12, 2017
Revised: June 8, 2017
Published online: July 11, 2017

